Tracking the Catalyst Layer Depth-Dependent Electrochemical Degradation of a Bimodal Pt/C Fuel Cell Catalyst: A Combined *Operando* Small- and Wide-Angle X-Ray Scattering Study

Johanna Schröder,[a] Rebecca K. Pittkowski,[a,b] Isaac Martens,[c] Raphael Chattot,[c] Jakub Drnec,[c] Jonathan Quinson,[b] Jacob J. K. Kirkensgaard,[d,e] Matthias Arenz[a*]

[a] Department of Chemistry and Biochemistry, University of Bern, Freiestrasse 3, 3012 Bern, Switzerland

[b] Department of Chemistry, University of Copenhagen, Universitetsparken 5, 2100 Copenhagen Ø, Denmark

[c] European Synchrotron Radiation Facility (ESRF), 71 Avenue des Martyrs, 38000 Grenoble, France

[d] Niels Bohr Institute, University of Copenhagen, Universitetsparken 5, 2100 København Ø, Denmark

[e] Department of Food Science, University of Copenhagen, Rolighedsvej 26, 1958 Frederiksberg, Denmark

[*] Corresponding author: matthias.arenz@dcb.unibe.ch

Abstract

The combination of *operando* small- and wide-angle X-ray scattering (SAXS, WAXS) is here presented to provide insights into the changes in mean particle sizes and phase fractions in fuel cell catalyst layers during accelerated stress tests (ASTs). As fuel cell catalyst, a bimodal Pt/C catalyst was chosen that consists of two distinguishable particle size populations. The presence of the two different sizes should favor and uncover electrochemical Ostwald ripening as degradation mechanism, i.e., the growth of larger particles in the Pt/C catalyst at the expense of the smaller particles via the formation of ionic metal species. However, instead of electrochemical Ostwald ripening, the results point toward classical Ostwald ripening via the local diffusion of metal atoms on the support. Furthermore, the grazing incidence mode provides insights into the catalyst layer depth-dependent degradation. While the larger particles show the same particle size changes close to the electrolyte-catalyst interface and within the catalyst layer, the smaller Pt nanoparticles exhibit a slightly decreased size at the electrolyte-catalyst interface. During the AST, both size populations increase in size, independent of the depth. Their phase fraction, i.e., the ratio of smaller to larger size population, however, exhibits a depth-dependent behavior. While at the electrolyte-catalyst interface the phase fraction of the smaller size population decreases, it increases in the inner catalyst layer. The results

of a depth-dependent degradation suggest that employing a depth-dependent catalyst design can be used for future improvement of catalyst stability.

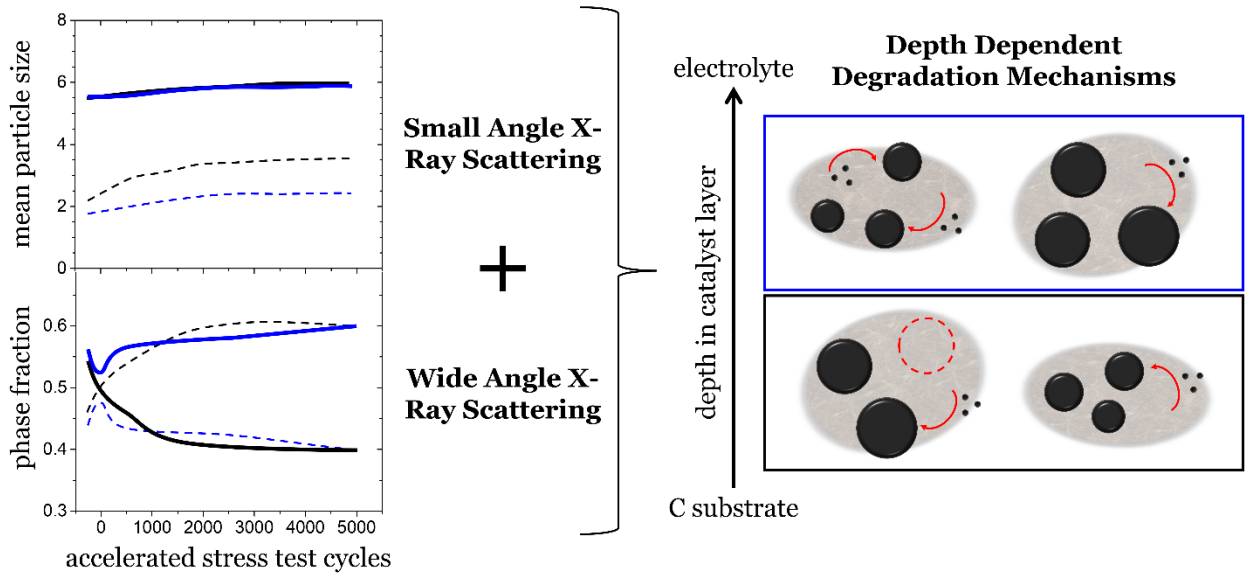

Keywords

Small-angle X-ray scattering (SAXS); wide-angle X-ray scattering (WAXS); fuel cell catalyst degradation; accelerated stress test (AST); bimodal Pt/C catalyst

1. Introduction

Proton exchange membrane fuel cells (PEMFCs) offer a sustainable alternative to conventional combustion engines.[1] Highly active precious metal based catalysts are typically used as state-of-the-art, e.g., PtCo catalysts in the Mirai vehicle from Toyota.[2] The translation of new PEMFC catalysts into their "real-life" application requires not only a high activity but also sufficient long-term catalyst stability of the costly catalyst.[3,4] Therefore, stability investigations and suitable degradation protocols to simulate realistic application conditions recently received increasing attention.[5–9] To reduce the time needed to induce catalyst degradation, accelerated stress tests (ASTs) are performed in fundamental screening studies.[10–13] The performed ASTs can induce different electrochemical degradation mechanisms that affect the nanoparticle (NP) size of the degrading catalyst: (1) migration of particles followed by coalescence, (2) metal dissolution, (3) electrochemical Ostwald ripening, and (4) particle detachment from the support.[14,15] While the electrochemical Ostwald ripening results in larger particles at the expense of smaller ones via the diffusion and redeposition of metal ions,[16–19] "classical" Ostwald ripening in heterogeneous catalysis involves the surface diffusion of atomic species on the support material leading to particle growth.[20–23] As a consequence, electrochemical

Ostwald ripening occurs at a macroscopic scale, whereas classical Ostwald ripening can be considered a local phenomenon.

The particle size of fuel cell catalysts is commonly determined by (scanning) transmission electron microscopy ((S)TEM). To observe the change of some specific particles before and after the treatment, identical location (IL) (S)TEM is performed.[24–32] In small-angle X-ray scattering (SAXS) studies the particle size change can be investigated in a larger catalyst volume comprising several thousands of nanoparticles as compared to the limited number of NPs and local characterization that is achieved by only (S)TEM.[33–38] For example, *ex situ* SAXS was recently performed after applying AST protocols in a gas diffusion electrode (GDE) setup[28,36,37] that eliminates mass transport limitations as compared to the rotating disk electrodes (RDEs) commonly used in fundamental research studies.[39] However, both (S)TEM and SAXS were not clearly demonstrating the degradation mechanism of electrochemical Ostwald ripening which has been considered as one of the main degradation mechanisms in membrane electrode assemblies (MEA).[5,10,40]

In the present study, the depth-dependent (in the following also referred to as z-direction, see Figure S1) degradation within a catalyst layer was investigated by combining *operando* SAXS and wide-angle X-ray scattering (WAXS). The aims were to reveal degradation phenomena such as electrochemical Ostwald ripening as well as to probe if the degradation is homogeneous within the catalyst layer. To generate a system that should favor electrochemical Ostwald ripening, a catalyst with two distinguishable Pt NP size distributions (bimodal catalyst) was prepared by mixing two commercial catalysts.[41]. Using an *operando* cell with grazing incidence configuration[42] at the ID31 beamline at the European Synchrotron Radiation Facility (ESRF) in Grenoble, load cycle conditions of PEMFCs were simulated as AST following a protocol recommended by the Fuel Cell Commercialization Conference of Japan (FCCJ).[12,43] In the separate analysis of *operando* SAXS and WAXS data, both techniques revealed different limitations in studying the change in size distributions of the bimodal catalyst. However, combining both SAXS and WAXS enabled determining the mean particle sizes as well as the respective phase fractions of the two populations. The mean particle sizes of both size populations were determined by SAXS, and those values were used as input for the Rietveld refinement of the WAXS data. Studying the degradation mechanism responsible for the typically observed increase in particle size, the results suggest a phenomenon in line with local Ostwald ripening via atom diffusion. The analysis of the depth-dependent degradation reveals that the behavior of the phase fraction between the populations of smaller and larger particles is different at the electrolyte-catalyst interface than in the inner catalyst film. This indicates that a depth-dependent design of catalyst layers could be an important strategy to improve catalyst stability.

2. Experimental section

2.1. Chemicals, materials, and gases

For the catalyst ink formation, ultrapure Milli-Q water (resistivity > 18.2 MΩ·cm, total organic carbon (TOC) < 5 ppb) from a Millipore system was used. Isopropanol (IPA, 99.7+ %, Alfa Aesar), commercial Pt/C catalysts (TEC10E20A (1-2 nm Pt/C, 19.4 wt% Pt) and TEC10E50E-HT (4-5 nm Pt/C, 50.6 wt% Pt), Tanaka kikinzoku kogyo), and Nafion dispersion (D1021, 10 wt. %, EW 1100, Fuel Cell Store) were used for the preparation of the catalyst ink. The working electrolyte (WE) was prepared using a gas diffusion layer (GDL) with a microporous layer (MPL) on top (Freudenberg H23C8, 0.230 µm thick). In the electrochemical measurements, diluted 70 % perchloric acid ($HClO_4$, suprapur, Sigma Aldrich) as the electrolyte and argon gas (BIP ultrahigh purity, Air Liquide) were used. The two commercial Pt/C catalysts were dispersed in ethanol (absolute, VWR) and drop cast on holey C support film of Cu 300 mesh grids (Quantifoil). The spectrochemical cell was cleaned by briefly immersing it in diluted Caro's acid at room temperature.

2.2. Catalyst synthesis and ink formation

The two commercial Pt/C catalysts (TEC10E20A and TEC10E50E-HT) were mixed in a Pt mass ratio of 0.4:0.6 to obtain the catalyst mixture with two size populations on different carbon (C) flakes (bimodal Pt/C catalyst). In the following, the two populations are referred to as the "smaller" and the "larger" size population, respectively. The catalyst mixture was dispersed in a mixture of Milli-Q water and IPA (water/IPA volume ratio of 3:1) to prepare about 5 mL of ink (Pt concentration of 0.5 mg/mL). To generate a suitable dispersion for further use, the mixture was sonicated for 5 min in a sonication bath (Bioblock Scientific, T 310/H, 35 kHz). After adding 38.5 µL of Nafion (Nafion/carbon mass ratio of 1), the dispersion was again sonicated for 5 min in a sonication bath.

2.3. Preparation of working electrode

The Freudenberg GDL was placed between a glass funnel and a sand core filter in a vacuum filtration setup. As described by Yarlagadda *et al.*[44] all this was placed on a collecting bottle. 4 mL of the prepared ink was diluted with 7 mL of Milli-Q water and 29 mL of IPA (water/IPA volume ratio of 1:3, Pt concentration of 0.05 mg/L). After 1 min of sonication in a sonication bath, the diluted ink was filled in a funnel. The catalyst was deposited on top of the GDL using a diaphragm vacuum pump (Vacuubrand, MZ 2C, max. 1.7 m^3/h and 9.0 mbar). The GDE was dried and stored in air. By this procedure, a nominal Pt loading of 0.208 mg/cm^2_{geo} was generated. For the electrochemical measurement, the GDE after vacuum filtration was cut in circles with a diameter of 1 cm.

2.3.1. Electrochemical cell and measurement

A transmission diffraction cell introduced before[42] was used with Ar saturated 0.1 M $HClO_4$ as electrolyte. The electrolyte was degassed in a bubbler before being introduced into the top of the cell, pumped out of the top of the cell, and recirculated back to the bubbler.

Activation of the catalyst was done by 10 cyclic voltammograms (CVs) between 0.06 and 1.0 V versus reversible hydrogen electrode (V_{RHE}) using a scan rate of 50 mV/s. ASTs applying potential steps between 0.6 and 1.0 V_{RHE} (3 s holding per potential) were performed, simulating load-cycle conditions in a fuel cell vehicle. In between the AST cycles, two CVs between 0.06 and 1.0 V_{RHE} were performed, see Table S1 for details of the measurement protocol. The decrease of the H_{upd} area was used as an *in-situ* tool for analyzing the level of degradation. However, the averaged H_{upd} of both populations of the bimodal catalyst does not help to distinguish the separate degradation of both populations.

2.4. Transmission electron microscopy (TEM)

TEM was performed with a Jeol 2100 microscope, operated at 200 kV. At least five different areas of the TEM grid were imaged at a minimum of three different magnifications. The NP diameter was determined by measuring at least 200 NPs with the imageJ software. The Pt/C catalysts were dispersed in ethanol and drop cast onto Quantifoil grids.

2.5. Small-angle X-ray scattering (SAXS)

The SAXS and WAXS pattern were collected with a 77.0 keV beam and reduced as described previously.[45] The beam size was focused to approximately 5 x 2 µm (horizontal x vertical). In grazing-incidence mode a depth profile was performed, see Figures S1 and S2 as an example. Three different depths were analyzed (referred to as depth 4, 8, and 12). Depth 4 was chosen as it is the first layer showing Pt pattern in WAXS, i.e., the layer closest to the electrolyte, and the SAXS pattern of depth 4 was analyzed using depth 3 as background. Depth 8 shows the maximum intensity in the SAXS diffraction i.e., the layer in the middle of the catalyst layer, and was analyzed using depth 18 as background. Depth 12 is deeper inside the catalyst layer and was analyzed using depth 18 as background.

After inserting electrolyte to the cell, the first scan was performed. To ensure that the surface of the particles was fully reduced, the cell was held at 0.6 V_{RHE} during X-ray data collection. Details about the measurement protocol during AST can be found in the SI, see Table S1.

The SAXS data analysis after background subtraction was performed as described previously[35,37,46–48] using a model of polydisperse spheres. The radially averaged intensity I(q) is expressed as a

function of the scattering vector $q = 4\pi \cdot \sin(\theta)/\lambda$, where λ is the wavelength and 2θ is the scattering angle. The background-corrected scattering data were fitted using a model of one or two polydisperse spheres described by a total volume distributed (i.e., volume-weighted) log-normal distribution. A hard-sphere form factor $F(R_2,\eta_2)$ was used.[49] The scattering data are fitted to the following expression:

$$I(q)= C_1 \cdot \int P_{s1}(q,R) V_1(R) D_1(R) dR + C_2 \cdot F(R_2,\eta_2) \int P_{s2}(q,R) V_2(R) D_2(R) dR$$

R is the particle radius, C_1 and C_2 are scaling constants, P_{s1} and P_{s2} the sphere form factors, V_1 and V_2 the particle volumes, and D_1 and D_2 the log-normal size distribution. The normalized sphere form factor is given by: [50,51]

$$P_s(q,R)= \left(3\frac{\sin(qR)-qR\cos(qR)}{(qR)^3}\right)^2$$

and the log-normal distribution by:

$$D(R)=\frac{1}{R\sigma\sqrt{2\pi}}\exp\left(\frac{-\left[\ln\left(\frac{R}{R_0}\right)\right]^2}{2\sigma^2}\right)$$

where σ is the variance and R_0 (evaluated in Å) the geometric mean of the log-normal distribution. The fitting was done using a home-written MATLAB code (available on request). The free parameters in the model are C_1, R_1, σ_1, C_2, R_2, σ_2, η_2. The values obtained for these parameters are reported in Table S2. To account for the two populations, the reported probability density functions were weighted by the relative surface contribution of the spheres (to point out the electrochemical contribution of the population) as detailed in the SI. Details about the determination of the mean particle sizes and deviation for the log-normal distributions are found in Table S2.

2.6. Wide-angle X-ray scattering (WAXS)

WAXS analysis was done by performing Rietveld refinement using GSAS-II,[52] as previously described.[42] The structural model used for refinement consisted of two platinum *fcc* phases (Fm-3m) of the same lattice constant *a*. The lattice constant was obtained from refinement with a single *fcc* phase (a = 3.9046(6)). The mean particle sizes obtained from SAXS were used as input parameters in the WAXS refinement as the volume-weighted average number of coherent scattering domains, which are calculated from the full-width-at-half-maximum of reflections refined with only Lorentzian line shapes.[42] In this approach, we assume that no strain effects contribute to the broadening of reflections in the diffraction pattern. The contribution of the instrumental profile to the broadening of the Bragg peaks can be neglected based on the refinement of the CeO_2 calibrant: For the ceria NIST standard (380 nm), the instrumental profile contributes less than 10 % to the width of the Bragg peaks. Therefore, no instrumental profile correction was included for the Rietveld refinement of the

nanoparticles, as the effect is insignificant compared to the peak broadening from the platinum nanoparticles and a complex model is further needed to account for the cell geometry.[22] The background was described by a diffraction pattern from the grazing incident scan with minimal platinum content (depth 3) to describe the carbon background correctly.

The phase fraction is determined based on the crystallite sizes used as input values during the Rietveld refinement, which is not identical to the SAXS mean particle size. Therefore, we studied the influence of slight variations of the input values of the crystallite sizes. The input domain sizes were shifted by ± 0.5 or ± 1.0 nm in three different ways in the WAXS refinement of the diffraction pattern of different depths, see Figures S7 and S8. First, the mean particle size of the larger size population is changed by ± 0.5 and ± 1.0 nm while the size of the smaller size population is kept constant. Second, the size of the larger size population is kept constant while the size of the smaller population is changed by ± 0.5 nm. Third, the sizes of both populations are changed at the same time in the same direction by ± 0.5 nm. The fractions obtained by varying the input domain sizes are found in Figure S7 and S8. These tests confirmed that the observed trend for the change in the two particle size population fractions is not an artifact of using the input of mean particle sizes from the SAXS fitting as the crystallite size. Details about the WAXS measurement protocol during AST are found in Table S1.

3. Results and discussion

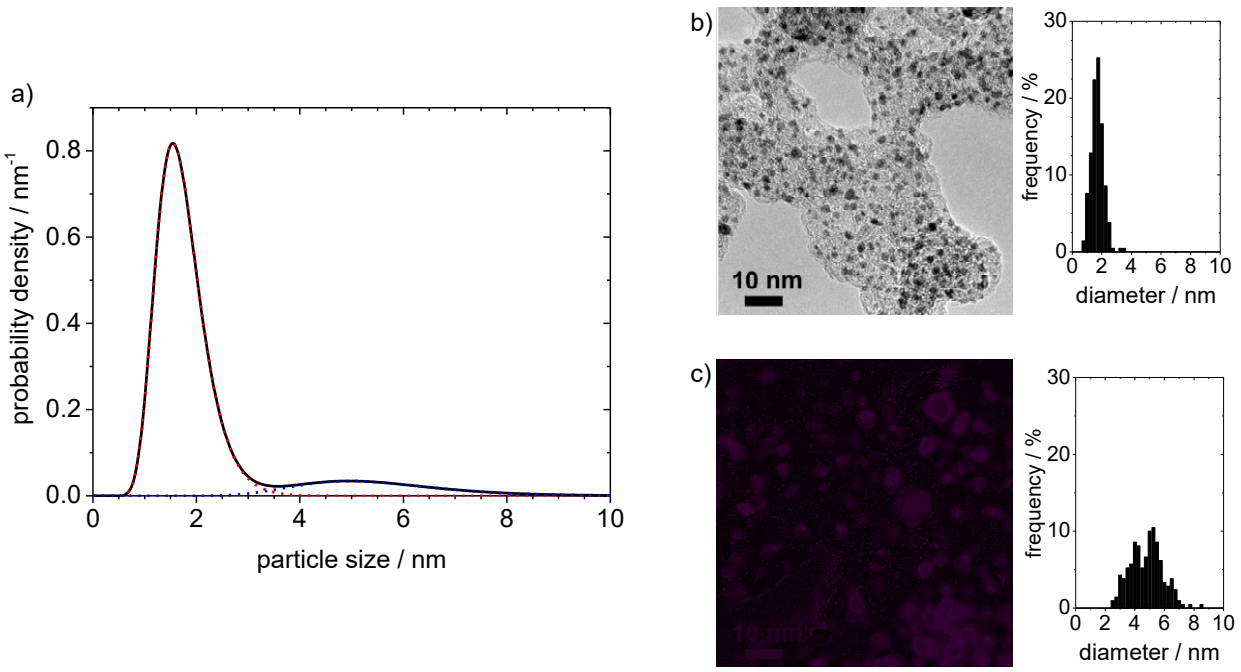

Figure 1. a) Calculated probability density function of the particle size of the bimodal catalyst after electrolyte insertion (black line) together with the probability densities of the separate size populations (dashed red and blue lines of the small and large size population, respectively) in a depth close to the electrolyte-catalyst interface derived from the SAXS data. b) TEM micrographs and size histograms of the two individual Pt/C catalysts that were mixed to obtain the bimodal Pt/C catalyst.

The aim of this work is to investigate the depth-dependent degradation mechanism(s) within a Pt/C fuel cell catalyst layer subjected to simulated load-cycle conditions. As the main analytical tool, a combination of *operando* SAXS and WAXS was used to obtain precise information on the mean particle sizes and crystallite size fractions as a function of the duration of the AST protocol. To induce and uncover electrochemical Ostwald ripening, i.e., the growth of larger NPs at the expense of smaller ones via the formation of ionic metal species,[16–19] a bimodal Pt/C catalyst obtained by mixing two different commercial Pt/C catalysts with distinguishable size populations, was studied, see Figure 1. The use of the bimodal catalyst prepared by mixing two catalysts enables us to distinguish between local and macroscopic Ostwald ripening. In local Ostwald ripening, mainly described for heterogeneous catalysis, atomic metal species are formed that diffuse on the support material.[20–23] The particle growth in this local phenomenon can only occur on individual or connected carbon flakes This is in contrast to macroscopic Ostwald ripening where ionic metal species are formed that can diffuse on a macroscopic scale, as proven by the detection of reduced metal special in the membrane

of MEAs[53] or the detection of metal species in scanning flow cell measurements coupled to inductively coupled mass spectrometry (SFC ICP-MS).[54] Furthermore, the here applied grazing-incidence mode allows a straightforward selection not only of different spots at the same depth (same x-y planes) in the catalyst layer but additionally z-scans can be performed,[55] to investigate if the degradation depends on the distance of the NPs to the electrolyte-catalyst interface. See Figure S1 for a scheme of the x-, y-, and z-direction relative to the electrolyte-catalyst interface.

Before discussing the influence of the AST protocol on the catalyst particles, we first introduce the combination of SAXS and WAXS analysis based on the catalyst after inserting the electrolyte into the cell in a z-direction close to the electrolyte-catalyst interface, see grey scattering and diffraction data in Figure 2. Based on the fact that the bimodal Pt/C catalyst is the result of mixing two individually characterized Pt/C catalysts in a known metal ratio (0.4:0.6 based on metal weight percentage of the two catalysts), the determined mean particle sizes and phase fractions in the bimodal Pt/C catalysts can be compared to the expected values. The analysis shows that the mean particle size of both populations of the bimodal catalyst can be determined by SAXS data analysis with high accuracy. The particle diameters and their standard deviations retrieved from the log-normal distributions obtained from the SAXS data are 1.7 ± 0.5 and 5.5 ± 1.5 nm, see Figure 1a, Figure 3a, and Table S2 for details about the fitting parameters. Comparing the individual catalysts in Figure 1 with the prepared bimodal catalyst, it is demonstrated that the SAXS results are in good agreement with the TEM data of ca. 2 and ca. 5 nm average size. However, a quantitative analysis of the relative number of NPs in the two size populations is difficult. Although the expected relative number of NPs in the two size populations could be fitted to the SAXS data as well, in simulations the fit is ambiguous in this respect, i.e., no one-to-one correspondence between the intensities of the two populations of the same scattering data is found. It is important to note that this is not the case for the mean particle sizes, which remain similar in simulations of different phase fractions of the two populations.

To address this limitation, we took advantage of the WAXS data. The WAXS diffraction patterns clearly show the typical Bragg peaks of the platinum *fcc* phase which are convoluted with the signals of the carbon and polymer background at low 2θ angles, see Figure S2b. From an angular range of six 2θ onwards, the platinum reflections are virtually free of background and can readily be analyzed by Rietveld refinement.[55] Simultaneously varying both the fraction and crystallite size of the two populations of Pt NPs in the Rietveld refinement of WAXS data was not feasible due to the intertwining of these variables, as only one population with an average coherent domain size was obtained. Therefore, we used the mean particle size of the two populations derived by the SAXS fitting as pre-defined input values in the Rietveld refinement of the WAXS data. Two platinum phases of different coherent domain sizes (input of SAXS mean particle sizes) were used as the structural

model in the Rietveld refinement. Although the mean particle size derived from the SAXS fitting is not identical with the coherent domain size in diffraction, the two parameters are closely related.[42] In this way the fractions of the platinum phases, i.e., their mass ratios, can be determined for the two size populations of Pt NPs. A representative refinement showing the two platinum phases of the structural model with different crystallite sizes is depicted in Figure S6. The ratio of smaller to larger population of 0.44:0.56 in the sample after electrolyte insertion close to electrolyte-catalyst interface obtained from the combined SAXS and WAXS data analysis is in good agreement with the theoretical ratio of 0.4:0.6 expected from the sample preparation procedure, see Figure 3b. Thus, the combination of *operando* SAXS and WAXS data analysis allows to readily evaluate both the size evolution of the two size populations and the fractions of the two size platinum crystallite domains of the bimodal Pt/C catalyst.

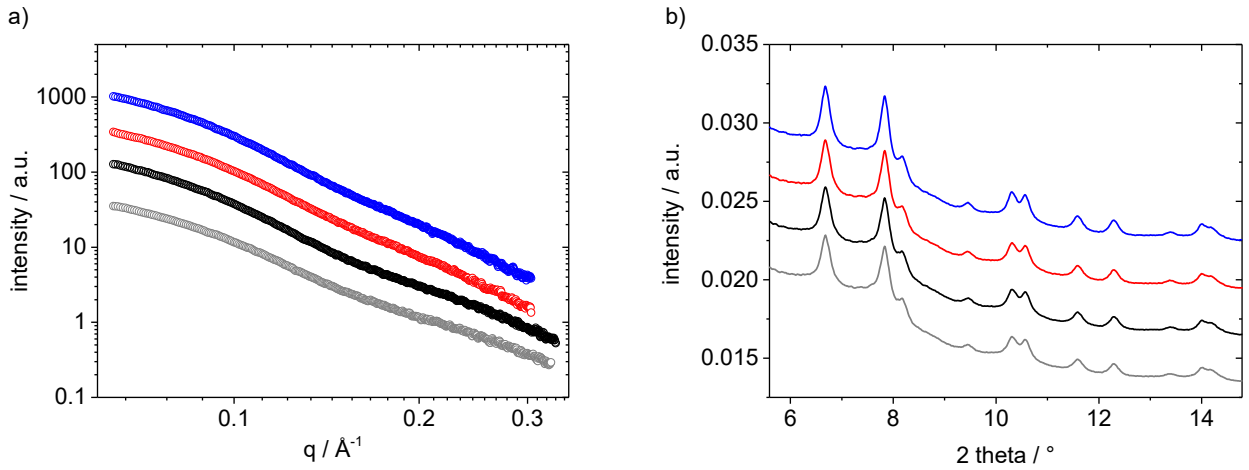

Figure 2. a) Background subtracted SAXS scattering data and b) WAXS diffractograms in an angular range from 5 to 15 ° 2 theta in the depth close to the electrolyte-catalyst interface: after electrolyte insertion (grey), after catalyst cleaning (black), after 2500 AST cycles (red), after 5000 AST cycles (blue). The increase of the height and narrowing of the peaks of the diffractogram during the AST protocol imply an increase in particle size, which is in agreement with the mean particle size results. The data in a) and b) are shown with a vertical offset to improve visibility of the different datasets.

At the beginning of the measurements and before starting the AST protocol, the Pt/C catalysts were first electrochemically contacted and thereafter exposed to a short cycling of the electrode potential. This procedure serves to confirm electrochemical contact of the catalyst as well as to clean it, see experimental section for details. It can be seen that already before the electrochemical contact (after electrolyte insertion), the initial particle size of the small population close to the electrolyte-catalyst interface appears to be slightly smaller as compared to the particle size of the same population at the

two other catalyst depths closer to the substrate-catalyst interface. At the same time, the particle size of the larger population is comparable throughout the different depths (see Figure 3a). Comparing the scattering data at two different positions of the same depth in the middle of the catalyst layer in Figure S3, it is confirmed that these observations are representative for the macroscopic catalyst layer, i.e., the changes in particle size of the two populations are identical at both x-y positions in the layer.

After applying cleaning CVs the fraction of the smaller NPs in the depth closest to the electrolyte-catalyst interface increases from 0.44:0.56 to 0.48:0.52 with respect to the larger size population, see Figure 3b, while the mean particle sizes remain unaffected as can be seen from the SAXS fitting, see Figure 3a. In this context, it is important to point out that refinement of the diffraction pattern yields a relative and not an absolute number for both populations. Hence, the increase in the fraction of the smaller size population can also be explained by a loss of the larger particles. Pt dissolution upon establishing electrochemical contact has been described by Pizzutilo *et al.*[8] by coupling scanning flow cells (SFC) with inductively coupled plasma mass spectrometry (ICP-MS). Our data suggest that this effect affects mostly the smaller Pt NPs that are located at the electrolyte-catalyst interface, whereas the larger size population seems not substantially affected. However, exposure of the catalyst to cleaning cycles seems to result in a particle loss phenomenon with a higher loss of NPs in the larger size population as evidenced by the change in phase fraction. A preferential detachment of the larger particles due to carbon corrosion would be in line with previous investigations by Mayrhofer *et al.*[10] and Hartl *et al.*[24] who demonstrated particle loss for the same catalyst that constitutes the larger fraction in the present work. Stronger support-particle interaction of the larger particles due to the larger contact area with the support, as compared to smaller ones, could lead to less detachment of larger NPs from the support.[56] However, the support-particle interaction is also determined by other factors, e.g., by the degree of graphitization of the carbon support that is difficult to rationalize for commercial catalysts.[18,57]

In the following, we now concentrate on the effect of the AST treatment on the catalyst, which is analyzed first at a depth close to the electrolyte-catalyst interface. Representative *operando* SAXS and WAXS data of the Pt/C catalyst after electrolyte insertion into the cell, after catalyst cleaning, after 2500, and after 5000 AST cycles are shown in Figure 2. Based on the mean particle size changes obtained from the SAXS data (see Figures S4 and S5, Table S2) three main observations are made, see Figure 3a. First, both populations of the catalyst located in the catalyst layer close to the electrolyte-catalyst interface increase in size. Second, at the beginning of the AST, the increase in size per treatment cycle is more pronounced than at the end of the AST. Third, the increase in mean particle size of the population of the larger particles is less pronounced (from 5.48 ± 1.45 to 5.87 ± 1.61 nm, size increase of around 7 %) than the size increase of the smaller particles (1.76 ± 0.48 to

2.42 ± 0.79, size increase of around 50 %), see Figure 3a. The observation of a more pronounced size increase at the beginning of the AST as compared to that during the AST is in line with previous findings.[3,8,26] The shifting of the average particle size of the smaller size population to larger values clearly indicates a preferential dissolution of smaller Pt NPs *within* the smaller size population that could be explained either by a local or macroscopic Ostwald ripening. However, the broadening of the size distribution (SAXS probability density function) during the AST is in better agreement with the local phenomenon of Ostwald ripening and thus an atomic diffusion process on the support. In the non-local Ostwald ripening, the re-deposition of Pt onto the larger size population should be highly favorable. The local, intra-population Ostwald ripening mechanism of the small population would be in agreement with atomic Pt species being mobile on the carbon support as previously proposed by Ferreira *et al.*[5] It seems that the diffusion of the soluble ionic Pt species does not lead to re-deposition in the catalyst layer and thus no macroscopic Ostwald ripening. Instead, in an MEA environment, Pt precipitation into the membrane can occur due to hydrogen crossover. In electrochemical measurements with liquid electrolyte, the ionic Pt species diffuse into the electrolyte and can be detected by SFC ICP-MS.[54] For the increase in average particle size of the larger size population, however, a distinction between either macroscopic or local Ostwald ripening, i.e., an inter- or intra-population particle growth is not feasible. Analyzing the change in phase fraction, it is seen that the phase fraction of the smaller size population decreases when applying the AST protocol. Such behavior is expected for several different degradation scenarios and therefore not interpreted further.

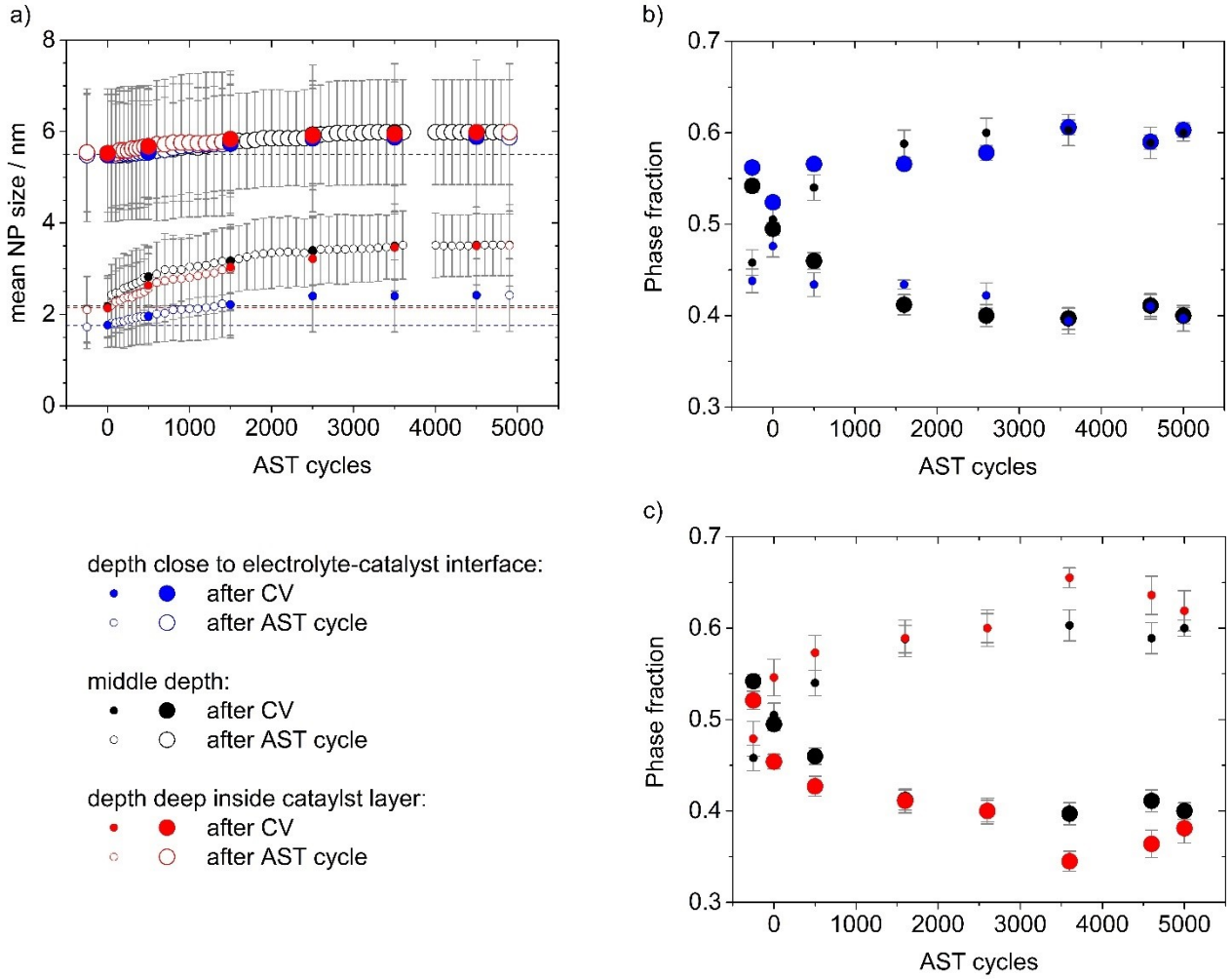

Figure 3. a) Mean particle size of the bimodal Pt NP/C catalyst (smaller and larger size population distinguished with smaller and larger circles) plotted together with the standard deviation of a log-normal distribution applying load-cycles conditions as AST protocol in an *operando* cell after the AST cycles (empty circles) and after CVs (filled circles) close to the electrolyte (blue), in the middle depth (black), and deeper inside the catalyst layer (red). Phase fractions of the two size populations (small and large circles, for the smaller and larger size populations, respectively) obtained from Rietveld refinement of the different depth keeping the particle sizes determined via SAXS constant, b) close to the electrolyte (blue) and in the middle catalyst layer (black), c) in the middle (black, data from Figure 2) and deeper inside the catalyst layer (red) (the red filled circles are placed in front of the red circles, due to an overlap the black circles are sometimes covered). The data points recorded after electrolyte insertion (before performing the cleaning CVs) are given on the x-axis for a negative AST number.

Trying to understand the depth dependence of the degradation, the changes of the particle size and the phase fraction were also analyzed in a "middle depth" of the catalyst layer, further away from the

electrolyte-catalyst interface. In Figure 3, it is seen that in both depths (close to the electrolyte-catalyst interface and in the middle catalyst depth) the mean particle size of both populations increases with the AST treatment. This confirms that the complete catalyst layer is electrochemically active and thus connected, see Figure 3a. Based on our observations, we can identify four common characteristics for the two depths analyzed. First, the particle size and the size change during the AST of the larger size population are similar in the two depths. Second, the particle size of the smaller size population increases in a more pronounced way than the particle size of the larger population (from 2.43 ± 0.67 to 3.52 ± 0.68 nm (size increase of around 45 %) and from 5.50 ± 1.17 to 5.99 ± 1.15 nm (size increase of around 9 %) in the middle catalyst layer depth). Third, the relative size increases of both populations are comparable in the depth close to the electrolyte-catalyst interface (7 and 50 % for the smaller and larger size population, see blue circles in Figure 3a) or in the middle of the catalyst layer (9 and 45 %, see black circles). Fourth, the particle size change of the larger size population seems to be independent of the depth.

As the width of the probability density of the smaller size population does not decrease, again no pure size-dependent Pt dissolution but the process of local Ostwald ripening occurs as described for the depth closer to the electrolyte-catalyst interface. However, there is also a distinct difference between the two depths. Comparing the depth-dependent phase fractions during the AST, it is seen that in the middle of the catalyst layer, the ratio of the smaller to the larger size population increases from the initial ratio of 0.51:0.49 measured after applying the cleaning procedure to reach a value of 0.6:0.4 at the end of treatment, see Figure 3b. Concomitantly, the particle sizes in both populations increase, see Figure 3a. This behavior of an increased phase fraction of the smaller in respect to the larger size population of the Pt/C catalyst in the middle of the catalyst layer is unexpected. It would be more intuitive to assume growth of the NPs and a decrease of the smaller NP fraction, as is observed at the electrolyte-catalyst interface. Therefore, we analyzed additional data obtained from a different z-direction at a third depth closer to the GDL, i.e., deeper inside the catalyst layer. The analysis of the SAXS and WAXS data in the depth far away from the electrolyte-catalyst interface shows the same unexpected results in change of the mean particle sizes and the phase fractions as observed in the middle catalyst layer, see Figure 3a and c.

To explain those observations, several scenarios can be considered. Enhanced dissolution of the larger particles seems to be unlikely. An increase of the amount of the smaller NPs in the catalyst layer further away from the electrolyte-catalyst due to carbon support corrosion and easier "travel through" the catalyst layer of the smaller NPs is also unlikely, as we found no indication of Pt NPs in the MPL during the AST, see Figure S2a. However, a preferential particle detachment as discussed above could explain the findings.

While it seems unlikely that a different degradation mechanism occurs inside the catalyst layer, it might be that only the ratio between the dissolution of the smaller size population and the particle detachment of the larger size population is changing. That is, while close to the electrolyte-catalyst interface the dissolution of the smaller population is more pronounced, deeper inside the catalyst layer the particle loss of the larger size population might be dominating. As a consequence, the phase fraction of the smaller size population decreases close to the electrolyte-catalyst interface, while it is increasing closer to the GDL, see Figure 4. The described degradation mechanism of Figure 4 might change in MEAs due to a membrane-catalyst interface (instead of the electrolyte-catalyst interface), however, the presented results point out the importance of depth-dependent degradation studies and the advantage of a bimodal catalyst.

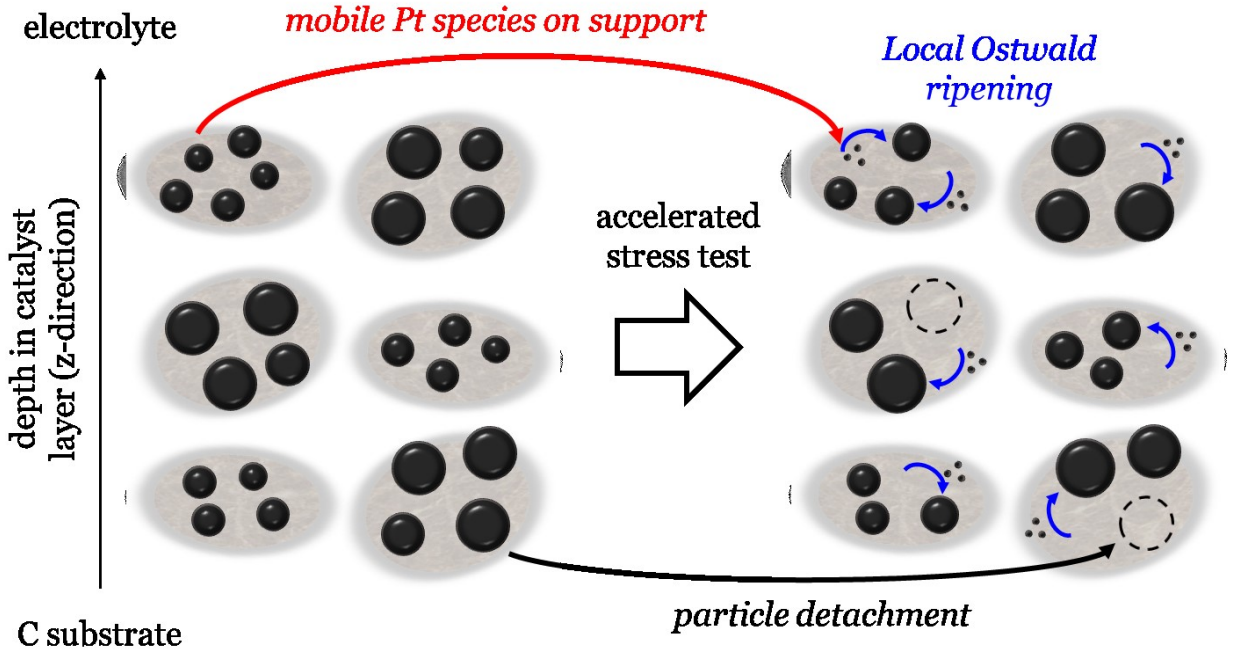

Figure 4. Scheme of the proposed depth-dependent degradation mechanism in the Pt/C catalyst.

4. Conclusion

The combination of *operando* SAXS and WAXS in grazing incidence configuration is used to investigate catalyst layer depth-dependent degradation of a fuel cell catalyst subjected to ASTs. A bimodal Pt/C catalyst was chosen that consists of two distinguishable particle size populations to maximize the chance to observe the expected electrochemical Ostwald ripening where the size of the larger particles in the Pt/C catalyst grows at the expense of the smaller particles via the deposition of metal ions. However, it is seen that the degradation mechanism is more complex. Establishing electrochemical contact inflicts the most pronounced degradation on smaller NPs close to the

electrolyte-catalyst interface. The initial cleaning cycles, by comparison, lead to particle detachment, a phenomenon particular pronounced one of the chosen heat-treated (the 'HT' from the commercial name implies a heat treatment (TEC10E50E-HT) which seems to lead to enhanced carbon corrosion at the NP-carbon interface) Pt/C catalysts with larger Pt NPs. The AST treatment, simulating load cycles, leads to features that can be associated with a preferential dissolution of smaller Pt particles and local Ostwald ripening via atomic Pt species mobile on the carbon support. The latter leads to intra-population particle growth. Concomitantly, the phase fraction between the smaller and the larger size population decreases at the electrolyte-catalyst interface, i.e., the number of NPs in the smaller fraction gets reduced with respect to the number of NPs in the larger fraction. Surprisingly, deeper in the catalyst layer the opposite trend is observed, i.e., the relative number of NPs in the smaller fraction increases. This indicates that deeper into the catalyst layer particle loss of the large fraction dominates. If one assumes that particle loss is equally likely throughout the catalyst layer, this would mean that dissolution and Ostwald ripening as well as other processes leading to intra-population particle growth is less pronounced in the catalyst layer than at the electrolyte-catalyst interface.

Supporting information

Details about the SAXS and WAXS measurement protocol, SAXS and WAXS raw data, details SAXS analysis and results, details WAXS analysis and results.

Notes

The Authors declare no competing financial interest.

Acknowledgements

This work was supported by the Swiss National Science Foundation (SNSF) via the project No. 200021_184742 and the Danish National Research Foundation Center for High Entropy Alloy Catalysis (CHEAC) DNRF-149. S. B. Simonsen and L. Theil Kuhn, Technical University of Denmark, are thanked for access to TEM. The authors also thank ESRF for beamtime at ID31 beamline and H. Isern and F. Russelo for technical support.

References

(1) Pollet, B. G.; Kocha, S. S.; Staffell, I. Current Status of Automotive Fuel Cells for Sustainable Transport. *Current Opinion in Electrochemistry*. Elsevier August 1, 2019, pp 90–95. https://doi.org/10.1016/j.coelec.2019.04.021.

(2) Yoshida, T.; Kojima, K. Toyota MIRAI Fuel Cell Vehicle and Progress Toward a Future

Hydrogen Society. *Electrochem. Soc. Interface* **2015**, *24* (2), 45–49. https://doi.org/10.1149/2.F03152if.

(3) Marcu, A.; Toth, G.; Kundu, S.; Colmenares, L. C.; Behm, R. J. Ex Situ Testing Method to Characterize Cathode Catalysts Degradation under Simulated Start-up/Shut-down Conditions – A Contribution to Polymer Electrolyte Membrane Fuel Cell Benchmarking. *J. Power Sources* **2012**, *215*, 266–273. https://doi.org/10.1016/j.jpowsour.2012.05.010.

(4) Katsounaros, I.; Cherevko, S.; Zeradjanin, A. R.; Mayrhofer, K. J. J. J. Oxygen Electrochemistry as a Cornerstone for Sustainable Energy Conversion. *Angew. Chemie - Int. Ed.* **2014**, *53* (1), 102–121. https://doi.org/10.1002/anie.201306588.

(5) Ferreira, P. J.; la O', G. J.; Shao-Horn, Y.; Morgan, D.; Makharia, R.; Kocha, S.; Gasteiger, H. A.; La O', G. J.; Shao-Horn, Y.; Morgan, D.; Makharia, R.; Kocha, S.; Gasteiger, H. A. Instability of Pt/C Electrocatalysts in Proton Exchange Membrane Fuel Cells. *J. Electrochem. Soc.* **2005**, *152* (11), A2256. https://doi.org/10.1149/1.2050347.

(6) Borup, R.; Meyers, J.; Pivovar, B.; Kim, Y. S.; Mukundan, R.; Garland, N.; Myers, D.; Wilson, M.; Garzon, F.; Wood, D.; Zelenay, P.; More, K.; Stroh, K.; Zawodzinski, T.; Boncella, J.; McGrath, J. E.; Inaba, M.; Miyatake, K.; Hori, M.; Ota, K.; Ogumi, Z.; Miyata, S.; Nishikata, A.; Siroma, Z.; Uchimoto, Y.; Yasuda, K.; Kimijima, K. I.; Iwashita, N. Scientific Aspects of Polymer Electrolyte Fuel Cell Durability and Degradation. *Chemical Reviews*. American Chemical Society October 2007, pp 3904–3951. https://doi.org/10.1021/cr0501821.

(7) Castanheira, L.; Silva, W. O.; Lima, F. H. B. B.; Crisci, A.; Dubau, L.; Maillard, F. Carbon Corrosion in Proton-Exchange Membrane Fuel Cells: Effect of the Carbon Structure, the Degradation Protocol, and the Gas Atmosphere. *ACS Catal.* **2015**, *5* (4), 2184–2194. https://doi.org/10.1021/cs501973j.

(8) Pizzutilo, E.; Geiger, S.; Grote, J.-P.; Mingers, A.; Mayrhofer, K. J. J.; Arenz, M.; Cherevko, S. On the Need of Improved Accelerated Degradation Protocols (ADPs): Examination of Platinum Dissolution and Carbon Corrosion in Half-Cell Tests. *J. Electrochem. Soc.* **2016**, *163* (14), F1510–F1514. https://doi.org/10.1149/2.0731614jes.

(9) Geiger, S.; Kasian, O.; Ledendecker, M.; Pizzutilo, E.; Mingers, A. M.; Fu, W. T.; Diaz-Morales, O.; Li, Z.; Oellers, T.; Fruchter, L.; Ludwig, A.; Mayrhofer, K. J. J.; Koper, M. T. M.; Cherevko, S. The Stability Number as a Metric for Electrocatalyst Stability Benchmarking. *Nat. Catal.* **2018**, *1* (7), 508–515. https://doi.org/10.1038/s41929-018-0085-6.

(10) Mayrhofer, K. J. J.; Meier, J. C.; Ashton, S. J.; Wiberg, G. K. H.; Kraus, F.; Hanzlik, M.;

Arenz, M. Fuel Cell Catalyst Degradation on the Nanoscale. *Electrochem. commun.* **2008**, *10* (8), 1144–1147. https://doi.org/10.1016/j.elecom.2008.05.032.

(11) Zana, A.; Speder, J.; Reeler, N. E. A.; Vosch, T.; Arenz, M. Investigating the Corrosion of High Surface Area Carbons during Start/Stop Fuel Cell Conditions: A Raman Study. *Electrochim. Acta* **2013**, *114*, 455–461. https://doi.org/10.1016/j.electacta.2013.10.097.

(12) Ohma, A.; Shinohara, K.; Iiyama, A.; Yoshida, T.; Daimaru, A. Membrane and Catalyst Performance Targets for Automotive Fuel Cells by FCCJ Membrane, Catalyst, MEA WG. *ECS Trans.* **2011**, *41* (1), 775–784. https://doi.org/10.1149/1.3635611.

(13) Schröder, J.; Quinson, J.; Kirkensgaard, J.; Alinejad, S.; Mints, V.; Jensen, K.; Arenz, M. A New Approach to Probe the Degradation of Fuel Cell Catalysts Under Realistic Conditions: Combining Tests in a Gas Diffusion Electrode Setup with Small Angle X-Ray Scattering. *J. Electrochem. Soc.* **2020**. https://doi.org/10.26434/chemrxiv.12263804.

(14) Meier, J. C.; Galeano, C.; Katsounaros, I.; Topalov, A. A.; Kostka, A.; Schüth, F.; Mayrhofer, K. J. J. Degradation Mechanisms of Pt/C Fuel Cell Catalysts under Simulated Start–Stop Conditions. *ACS Catal.* **2012**, *2* (5), 832–843. https://doi.org/10.1021/cs300024h.

(15) Cherevko, S.; Kulyk, N.; Mayrhofer, K. J. J. Durability of Platinum-Based Fuel Cell Electrocatalysts: Dissolution of Bulk and Nanoscale Platinum. *Nano Energy* **2016**, *29*, 275–298. https://doi.org/10.1016/j.nanoen.2016.03.005.

(16) Redmond, P. L.; Hallock, A. J.; Brus, L. E. Electrochemical Ostwald Ripening of Colloidal Ag Particles on Conductive Substrates. *Nano Lett.* **2005**, *5* (1), 131–135. https://doi.org/10.1021/nl048204r.

(17) Virkar, A. V.; Zhou, Y. Mechanism of Catalyst Degradation in Proton Exchange Membrane Fuel Cells. *J. Electrochem. Soc.* **2007**, *154* (6), B540. https://doi.org/10.1149/1.2722563/XML.

(18) Shao-Horn, Y.; Sheng, W. C.; Chen, S.; Ferreira, P. J.; Holby, E. F.; Morgan, D. Instability of Supported Platinum Nanoparticles in Low-Temperature Fuel Cells. *Top. Catal.* **2007**, *46* (3–4), 285–305. https://doi.org/10.1007/s11244-007-9000-0.

(19) Parthasarathy, P.; Virkar, A. V. Electrochemical Ostwald Ripening of Pt and Ag Catalysts Supported on Carbon. *J. Power Sources* **2013**, *234*, 82–90. https://doi.org/10.1016/j.jpowsour.2013.01.115.

(20) Simonsen, S. B.; Chorkendorff, I.; Dahl, S.; Skoglundh, M.; Sehested, J.; Helveg, S. Ostwald Ripening in a Pt/SiO2 Model Catalyst Studied by in Situ TEM. *J. Catal.* **2011**, *281* (1), 147–155. https://doi.org/10.1016/j.jcat.2011.04.011.

(21) Simonsen, S. B.; Chorkendorff, I.; Dahl, S.; Skoglundh, M.; Meinander, K.; Jensen, T. N.;

Lauritsen, J. V.; Helveg, S. Effect of Particle Morphology on the Ripening of Supported Pt Nanoparticles. *J. Phys. Chem. C* **2012**, *116* (9), 5646–5653. https://doi.org/10.1021/jp2098262.

(22) Kistamurthy, D.; Saib, A. M.; Moodley, D. J.; Niemantsverdriet, J. W.; Weststrate, C. J. Ostwald Ripening on a Planar Co/SiO2 Catalyst Exposed to Model Fischer–Tropsch Synthesis Conditions. *J. Catal.* **2015**, *328*, 123–129. https://doi.org/10.1016/j.jcat.2015.02.017.

(23) Bett, J. A. S.; Kinoshita, K.; Stonehart, P. Crystallite Growth of Platinum Dispersed on Graphitized Carbon Black II. Effect of Liquid Environment. *J. Catal.* **1976**, *41* (1), 124–133. https://doi.org/10.1016/0021-9517(76)90207-4.

(24) Hartl, K.; Hanzlik, M.; Arenz, M. IL-TEM Investigations on the Degradation Mechanism of Pt/C Electrocatalysts with Different Carbon Supports. *Energy Environ. Sci.* **2011**, *4* (1), 234–238. https://doi.org/10.1039/C0EE00248H.

(25) Hodnik, N.; Zorko, M.; Bele, M.; Hočevar, S.; Gaberšček, M. Identical Location Scanning Electron Microscopy: A Case Study of Electrochemical Degradation of PtNi Nanoparticles Using a New Nondestructive Method. *J. Phys. Chem. C* **2012**, *116* (40), 21326–21333. https://doi.org/10.1021/jp303831c.

(26) Zana, A.; Speder, J.; Roefzaad, M.; Altmann, L.; Baumer, M.; Arenz, M.; Bäumer, M.; Arenz, M. Probing Degradation by IL-TEM: The Influence of Stress Test Conditions on the Degradation Mechanism. *J. Electrochem. Soc.* **2013**, *160* (6), F608–F615. https://doi.org/10.1149/2.078306jes.

(27) Arenz, M.; Zana, A. Fuel Cell Catalyst Degradation: Identical Location Electron Microscopy and Related Methods. *Nano Energy* **2016**, *29*, 299–313. https://doi.org/10.1016/j.nanoen.2016.04.027.

(28) Alinejad, S.; Inaba, M.; Schröder, J.; Du, J.; Quinson, J.; Zana, A.; Arenz, M. Testing Fuel Cell Catalysts under More Realistic Reaction Conditions: Accelerated Stress Tests in a Gas Diffusion Electrode Setup. *J. Phys. Energy* **2020**, *2* (2), 024003. https://doi.org/10.1088/2515-7655/ab67e2.

(29) Schonvogel, D.; Hülstede, J.; Wagner, P.; Kruusenberg, I.; Tammeveski, K.; Dyck, A.; Agert, C.; Wark, M. Stability of Pt Nanoparticles on Alternative Carbon Supports for Oxygen Reduction Reaction. *J. Electrochem. Soc.* **2017**, *164* (9), F995. https://doi.org/10.1149/2.1611709JES.

(30) Souza, N. E.; Bott-Neto, J. L.; Rocha, T. A.; da Silva, G. C.; Teixeira-Neto, E.; Gonzalez, E. R.; Ticianelli, E. A. Support Modification in Pt/C Electrocatalysts for Durability Increase: A

Degradation Study Assisted by Identical Location Transmission Electron Microscopy. *Electrochim. Acta* **2018**, *265*, 523–531. https://doi.org/10.1016/J.ELECTACTA.2018.01.180.

(31) Lafforgue, C.; Maillard, F.; Martin, V.; Dubau, L.; Chatenet, M. Degradation of Carbon-Supported Platinum-Group-Metal Electrocatalysts in Alkaline Media Studied by in Situ Fourier Transform Infrared Spectroscopy and Identical-Location Transmission Electron Microscopy. *ACS Catal.* **2019**, 5613–5622. https://doi.org/10.1021/acscatal.9b00439.

(32) Yu, H.; Zachman, M.; Myers, D.; Mukundan, R.; Zhang, H.; Zelenay, P.; Neyerlin, K.; Cullen, D. Elucidating Fuel Cell Catalyst Degradation Mechanisms by Identical-Location Transmission Electron Microscopy. *Microsc. Microanal.* **2021**, *27* (S1), 974–976. https://doi.org/10.1017/S1431927621003706.

(33) Speder, J.; Zana, A.; Spanos, I.; Kirkensgaard, J. J. K. K.; Mortensen, K.; Hanzlik, M.; Arenz, M. Comparative Degradation Study of Carbon Supported Proton Exchange Membrane Fuel Cell Electrocatalysts - The Influence of the Platinum to Carbon Ratio on the Degradation Rate. *J. Power Sources* **2014**, *261*, 14–22. https://doi.org/10.1016/j.jpowsour.2014.03.039.

(34) Inaba, M.; Quinson, J.; Arenz, M. PH Matters: The Influence of the Catalyst Ink on the Oxygen Reduction Activity Determined in Thin Film Rotating Disk Electrode Measurements. *J. Power Sources* **2017**, *353*, 19–27. https://doi.org/10.1016/j.jpowsour.2017.03.140.

(35) Quinson, J.; Inaba, M.; Neumann, S.; Swane, A. A.; Bucher, J.; Simonsen, S. B.; Theil Kuhn, L.; Kirkensgaard, J. J. K.; Jensen, K. M. Ø.; Oezaslan, M.; Kunz, S.; Arenz, M. Investigating Particle Size Effects in Catalysis by Applying a Size-Controlled and Surfactant-Free Synthesis of Colloidal Nanoparticles in Alkaline Ethylene Glycol: Case Study of the Oxygen Reduction Reaction on Pt. *ACS Catal.* **2018**, *8* (7), 6627–6635. https://doi.org/10.1021/acscatal.8b00694.

(36) Schröder, J.; Quinson, J.; Mathiesen, J. K.; Kirkensgaard, J. J. K.; Alinejad, S.; Mints, V. A.; Jensen, K. M. ∅.; Arenz, M. A New Approach to Probe the Degradation of Fuel Cell Catalysts under Realistic Conditions: Combining Tests in a Gas Diffusion Electrode Setup with Small Angle X-Ray Scattering. *J. Electrochem. Soc.* **2020**, *167* (13), 134515. https://doi.org/10.1149/1945-7111/abbdd2.

(37) Alinejad, S.; Quinson, J.; Schröder, J.; Kirkensgaard, J. J. K.; Arenz, M. Carbon-Supported Platinum Electrocatalysts Probed in a Gas Diffusion Setup with Alkaline Environment: How Particle Size and Mesoscopic Environment Influence the Degradation Mechanism. *ACS Catal.* **2020**, *10* (21), 13040–13049. https://doi.org/10.1021/acscatal.0c03184.

(38) Binninger, T.; Garganourakis, M.; Han, J.; Patru, A.; Fabbri, E.; Sereda, O.; Kötz, R.; Menzel, A.; Schmidt, T. J. Particle-Support Interferences in Small-Angle X-Ray Scattering from Supported-Catalyst Materials. *Phys. Rev. Appl.* **2015**, *3* (2), 024012(6). https://doi.org/10.1103/PhysRevApplied.3.024012.

(39) Ehelebe, K.; Seeberger, D.; Paul, M. T. Y.; Thiele, S.; Mayrhofer, K. J. J.; Cherevko, S. Evaluating Electrocatalysts at Relevant Currents in a Half-Cell: The Impact of Pt Loading on Oxygen Reduction Reaction. *J. Electrochem. Soc.* **2019**, *166* (16), F1259–F1268. https://doi.org/10.1149/2.0911915jes.

(40) Speder, J.; Zana, A.; Spanos, I.; Kirkensgaard, J. J. K.; Mortensen, K.; Hanzlik, M.; Arenz, M. Comparative Degradation Study of Carbon Supported Proton Exchange Membrane Fuel Cell Electrocatalysts - The Influence of the Platinum to Carbon Ratio on the Degradation Rate. *J. Power Sources* **2014**, *261*, 14–22. https://doi.org/10.1016/j.jpowsour.2014.03.039.

(41) Quinson, J.; Röefzaad, M.; Deiana, D.; Hansen, T. W.; Wagner, J. B.; Nesselberger, M.; Crampton, A. S.; Ridge, C. J.; Schweinberger, F. F.; Heiz, U.; Arenz, M. Electrochemical Stability of Subnanometer Pt Clusters. *Electrochim. Acta* **2018**, *277*, 211–217. https://doi.org/10.1016/j.electacta.2018.04.211.

(42) Martens, I.; Chattot, R.; Rasola, M.; Blanco, M. V.; Honkimäki, V.; Bizzotto, D.; Wilkinson, D. P.; Drnec, J. Probing the Dynamics of Platinum Surface Oxides in Fuel Cell Catalyst Layers Using in Situ X-Ray Diffraction. *ACS Appl. Energy Mater.* **2019**, *2* (11), 7772–7780. https://doi.org/10.1021/acsaem.9b00982.

(43) Park, Y.-C.; Kakinuma, K.; Uchida, M.; Tryk, D. A.; Kamino, T.; Uchida, H.; Watanabe, M. Investigation of the Corrosion of Carbon Supports in Polymer Electrolyte Fuel Cells Using Simulated Start-up/Shutdown Cycling. *Electrochim. Acta* **2013**, *91*, 195–207. https://doi.org/10.1016/j.electacta.2012.12.082.

(44) Yarlagadda, V.; McKinney, S. E.; Keary, C. L.; Thompson, L.; Zulevi, B.; Kongkanand, A. Preparation of PEMFC Electrodes from Milligram-Amounts of Catalyst Powder. *J. Electrochem. Soc.* **2017**, *164* (7), F845–F849. https://doi.org/10.1149/2.1461707jes.

(45) Martens, I.; Vamvakeros, A.; Martinez, N.; Chattot, R.; Pusa, J.; Blanco, M. V.; Fisher, E. A.; Asset, T.; Escribano, S.; Micoud, F.; Starr, T.; Coelho, A.; Honkimäki, V.; Bizzotto, D.; Wilkinson, D. P.; Jacques, S. D. M.; Maillard, F.; Dubau, L.; Lyonnard, S.; Morin, A.; Drnec, J. Imaging Heterogeneous Electrocatalyst Stability and Decoupling Degradation Mechanisms in Operating Hydrogen Fuel Cells. *ACS Energy Lett.* **2021**, *6* (8), 2742–2749. https://doi.org/10.1021/acsenergylett.1c00718.

(46) Schröder, J.; Quinson, J.; Mathiesen, J. K.; Kirkensgaard, J. J. K.; Alinejad, S.; Mints, V. A.;

Jensen, K. M. Ø.; Arenz, M. A New Approach to Probe the Degradation of Fuel Cell Catalysts under Realistic Conditions: Combining Tests in a Gas Diffusion Electrode Setup with Small Angle X-Ray Scattering. *J. Electrochem. Soc.* **2020**, *167* (13), 134515. https://doi.org/10.1149/1945-7111/abbdd2.

(47) Speder, J.; Altmann, L.; Roefzaad, M.; Bäumer, M.; Kirkensgaard, J. J. K. K.; Mortensen, K.; Arenz, M. Pt Based PEMFC Catalysts Prepared from Colloidal Particle Suspensions – a Toolbox for Model Studies. *Phys. Chem. Chem. Phys.* **2013**, *15* (10), 3602. https://doi.org/10.1039/c3cp50195g.

(48) Schröder, J.; Mints, V. A.; Bornet, A.; Berner, E.; Fathi Tovini, M.; Quinson, J.; Wiberg, G. K. H.; Bizzotto, F.; El-Sayed, H. A.; Arenz, M. The Gas Diffusion Electrode Setup as Straightforward Testing Device for Proton Exchange Membrane Water Electrolyzer Catalysts. *JACS Au* **2021**, *1* (3), 247–251. https://doi.org/10.1021/jacsau.1c00015.

(49) Zemb, T.; Lindner, P. *Neutron, X-Rays and Light. Scattering Methods Applied to Soft Condensed Matter*, 1st ed.; Elsevier: Amsterdam, 2002.

(50) Kajiwara, K.; Hiragi, Y. Chapter 6 Structure Analysis by Small-Angle X-Ray Scattering. *Anal. Spectrosc. Libr.* **1996**, *7* (C), 353–404. https://doi.org/10.1016/S0926-4345(96)80007-1.

(51) Garcia, P. R. A. F.; Prymak, O.; Grasmik, V.; Pappert, K.; Wlysses, W.; Otubo, L.; Epple, M.; Oliveira, C. L. P. An in Situ SAXS Investigation of the Formation of Silver Nanoparticles and Bimetallic Silver–Gold Nanoparticles in Controlled Wet-Chemical Reduction Synthesis. *Nanoscale Adv.* **2020**, *2* (1), 225–238. https://doi.org/10.1039/C9NA00569B.

(52) Toby, B. H.; Von Dreele, R. B. GSAS-II : The Genesis of a Modern Open-Source All Purpose Crystallography Software Package. *J. Appl. Crystallogr.* **2013**, *46* (2), 544–549. https://doi.org/10.1107/S0021889813003531.

(53) Ohma, A.; Suga, S.; Yamamoto, S.; Shinohara, K. Membrane Degradation Behavior during Open-Circuit Voltage Hold Test. *J. Electrochem. Soc.* **2007**, *154* (8), B757. https://doi.org/10.1149/1.2741129.

(54) Topalov, A. A.; Cherevko, S.; Zeradjanin, A. R.; Meier, J. C.; Katsounaros, I.; Mayrhofer, K. J. J. Towards a Comprehensive Understanding of Platinum Dissolution in Acidic Media. *Chem. Sci.* **2014**, *5* (2), 631–638. https://doi.org/10.1039/C3SC52411F.

(55) Martens, I.; Vamvakeros, A.; Chattot, R.; Blanco, M. V.; Rasola, M.; Pusa, J.; Jacques, S. D. M.; Bizzotto, D.; Wilkinson, D. P.; Ruffmann, B.; Heidemann, S.; Honkimäki, V.; Drnec, J. X-Ray Transparent Proton-Exchange Membrane Fuel Cell Design for in Situ Wide and Small

Angle Scattering Tomography. *J. Power Sources* **2019**, *437*, 226906. https://doi.org/10.1016/j.jpowsour.2019.226906.

(56) Kregar, A.; Kravos, A.; Katrašnik, T. Methodology for Evaluation of Contributions of Ostwald Ripening and Particle Agglomeration to Growth of Catalyst Particles in PEM Fuel Cells. *Fuel Cells* **2020**, *20* (4), 487–498. https://doi.org/10.1002/fuce.201900208.

(57) Schlögl, K.; Hanzlik, M.; Arenz, M. Comparative IL-TEM Study Concerning the Degradation of Carbon Supported Pt-Based Electrocatalysts. *J. Electrochem. Soc.* **2012**, *159* (6), B677–B682. https://doi.org/10.1149/2.035206jes.